COMMUNICATION

Check for updates

Pressure-induced non-radiative losses in halide perovskite light-emitting diodes†‡

Young-Kwang Jung, [ID] §[a] Mayami Abdulla,§[b] Richard H. Friend,§[b] Samuel D. Stranks [ID] §*[bc] and Aron Walsh [ID] *[d]

The control of non-radiative losses in light-emitting diodes (LEDs) based on metal halide perovskites is crucial to improve device efficiency. Recent studies have shown a correlation between lattice strain and electron–hole recombination. To consolidate the concept, we investigate how external pressure (strain) affects the crystal structure, electronic properties, point defect concentration, and luminescence efficiency of $CH_3NH_3PbBr_3$. Relativistic first-principles calculations reveal enhanced Rashba splitting and Schottky defect disorder under compression, which produce a pronounced decrease in the electroluminescence peak energy and intensity in operating $CH_3NH_3PbBr_3$ LEDs. The resulting model sheds light on the factors underpinning the intricate strain–property relationships in soft crystalline semiconductors.

Applications of halide perovskite semiconductors have ranged from photovoltaic (PV) to light-emitting diodes (LED) applications.[1–4] Although both power conversion efficiency of perovskite PV and external quantum efficiency of LEDs have reached over 20%,[5–8] these are still well below their theoretical limits. Non-radiative carrier recombination – which generates heat rather than light – in the active perovskite layer is one of the key factors that diminishes the efficiency of both LED and PV devices.[9] Non-radiative recombination has several origins;

for instance, indirect band to band transitions or defect mediated recombination (*i.e.* Shockley–Read–Hall recombination).[10]

There have been recent insights into how the strain present in halide perovskite films affects non-radiative recombination and luminescence efficiency.[11,12] Strain – which can develop within the film during the growth and crystallization process – exhibits complex heterogeneity patterns that extend across multiple length scales in perovskite films and is demonstrated by spatial variation in luminescence.[13] Spacial correlation between lattice strain and photoluminescence (PL) lifetime was directly revealed even in high-quality perovskite thin films.[14] A recent study by Kim *et al.*[15] reported that relieving the strain by cation exchange could reduce trap density and suppress non-radiative recombination, which results in higher open-circuit voltage of perovskite PV devices. Another study by Ye *et al.*[16] also has demonstrated that strain relaxation in perovskite solar cells displayed an 1.2 times higher PCE and considerably longer stability than control groups. Nonetheless, the defect species that strongly couple with the strain in halide perovskites, and the other factors that could lead to non-radiative recombination, are poorly understood.

Herein, we aim to better understand the relationship between strain and carrier recombination. We set pressure as the sole control variable as it is a thermodynamic parameter that can directly induce strain in materials and tune their properties. Operando experiments of $CH_3NH_3PbBr_3$ (or $MAPbBr_3$) perovskite LED were performed to probe the change in the device properties (*i.e.* electroluminescence, EL) under hydrostatic pressure. The measurements were performed with the device immersed in an inert fluid (Fluorinert) acting as a pressure transmitting inside a capillary high-pressure cell. Next, complementary first-principles density functional theory (DFT) calculations were performed to demonstrate a change in material properties (atomic structure and electronic structure) at each pressure point. Finally, we adopted a statistical thermo-dynamic model to describe how defect concentration (including Schottky and Frenkel disorders) changes as pressure is applied. Our unique approach employs the pressure dependence of EL in

[a] *Department of Materials Science and Engineering, Yonsei University, Seoul 03722, Korea. E-mail: sds65@cam.ac.uk*

[b] *Cavendish Laboratory, University of Cambridge, JJ Thompson Avenue, Cambridge CB3 0HE, UK*

[c] *Department of Chemical Engineering & Biotechnology, University of Cambridge, Philippa Fawcett Drive, Cambridge, CB3 0AS, UK*

[d] *Department of Materials, Imperial College London, Exhibition Road, London, SW7 2AZ, UK. E-mail: a.walsh@imperial.ac.uk*

† The crystal structure files for the optimised pristine and defective materials have been made available in an on-line repository at **https://doi.org/10.5281/zenodo.7006160**

‡ Electronic supplementary information (ESI) available: *J–V* curves of a device under pressure, EL spectra while pressure is released, changes in deformation potential, 3D band structure, and charge correction term as a function of pressure. See DOI: **https://doi.org/10.1039/d2tc01490d**

§ Contributed equally to this work.

12560 | *J. Mater. Chem. C*, 2022, **10**, 12560–12568

This journal is © The Royal Society of Chemistry 2022

perovskite devices to elucidate the pressure-carrier recombination relationship. The analysis provides insights into the strain–structure–property relationships of halide perovskites.

Results and discussion

The EL evolution of a MAPbBr$_3$ device measured under the application of various external hydrostatic pressures is shown in Fig. 1. All EL spectra are normalised to the number of counts per second per mA and were collated at room temperature. The MAPbBr$_3$ LED is fabricated following Ref. 17 which under ambient conditions ($T \cong 298$ K, $P \cong 1$ atm) demonstrates green EL with a peak wavelength of $\lambda_{max} = 540$ nm (see Methods for device stack). The evolution of the LED EL intensity with varying pressure is depicted in Fig. 1a. These results demonstrate that the intensity is impaired as the pressure rises; however EL intensity rapidly diminishes with the first increment of pressure. The reduction in EL intensity confirms that

pressure adversely impacts the output of the MAPbBr$_3$ LEDs. The fact there is no significant inhibition in charge injection to the device when the pressure is applied (see Fig. S1, ESI‡) allows us to assume that an increase in non-radiative recombination is the main cause of the EL reduction.

The EL spectra have been normalised to the intensity value at the emission peak in Fig. 1b. The peak energy gradually shifts to longer wavelengths (lower energies) at a rate of 7 meV kbar^{-1} as the sample was compressed. Fig. 1c and d, demonstrate that the EL emission peak is negatively correlated with the applied pressure, indicating a pressure-induced band gap reduction. These results are consistent with previous studies of thin films and crystals of perovskite materials[18–21] that have shown the same trend in band gap pressure relation. In our case and within the studied range of pressure, the MAPbBr$_3$ LED proved to be considerably flexible in terms of band gap where the emission peak wavelength exhibited a gradual shift back to shorter wavelengths as the sample was decompressed slowly (see Fig. S2, ESI‡).
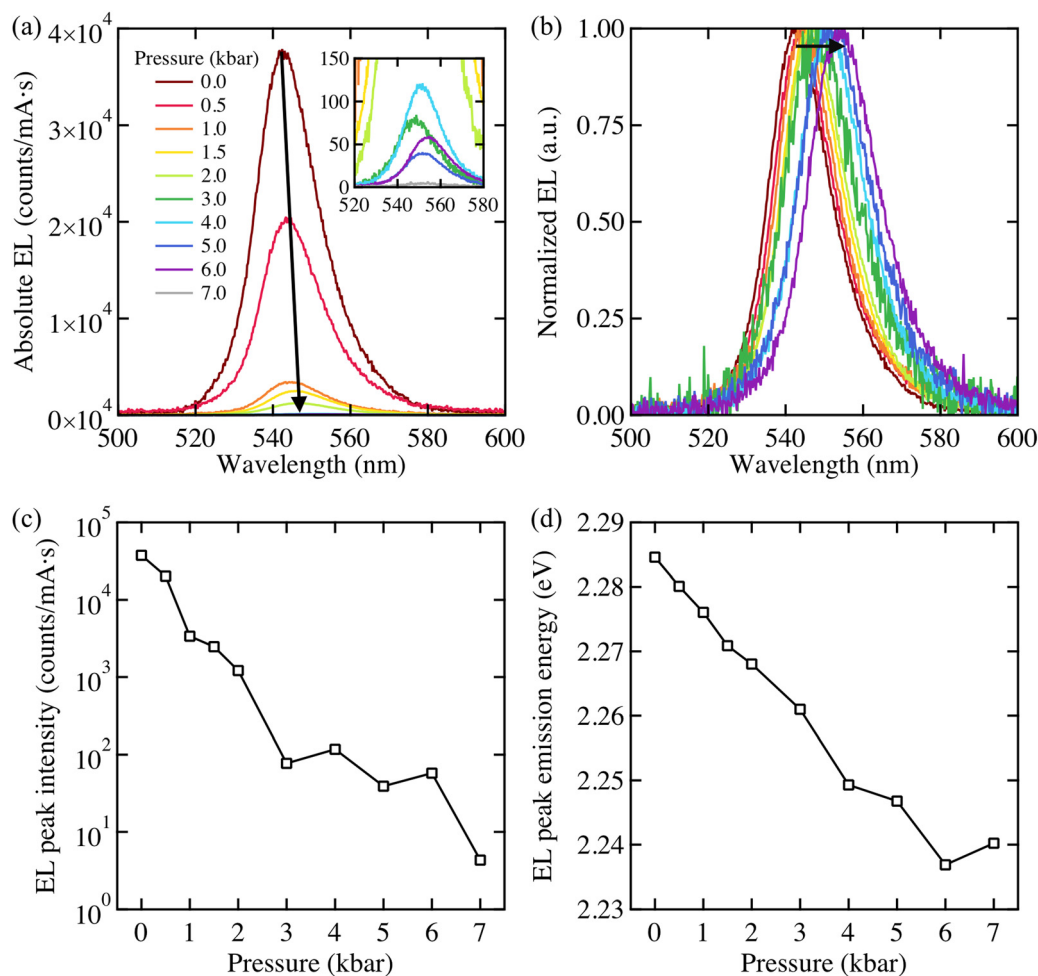
Fig. 1 Spectroscopic measurements of a MAPbBr$_3$ perovskite-based device operated at a constant current of 12 mA, under externally applied hydrostatic pressure within the range of 0 kbar $\leq P \leq$ 7 kbar at room temperature. (a) The measured electroluminescence (EL) spectra as a function of wavelength at different pressures. The EL intensity axis is shown in counts per second. (b) Normalised EL spectra as a function of wavelength. The black arrows in (a) and (b) show progression with increasing pressure. (c) The pressure dependence of EL peak intensity. (d) The pressure dependence of EL peak energy.
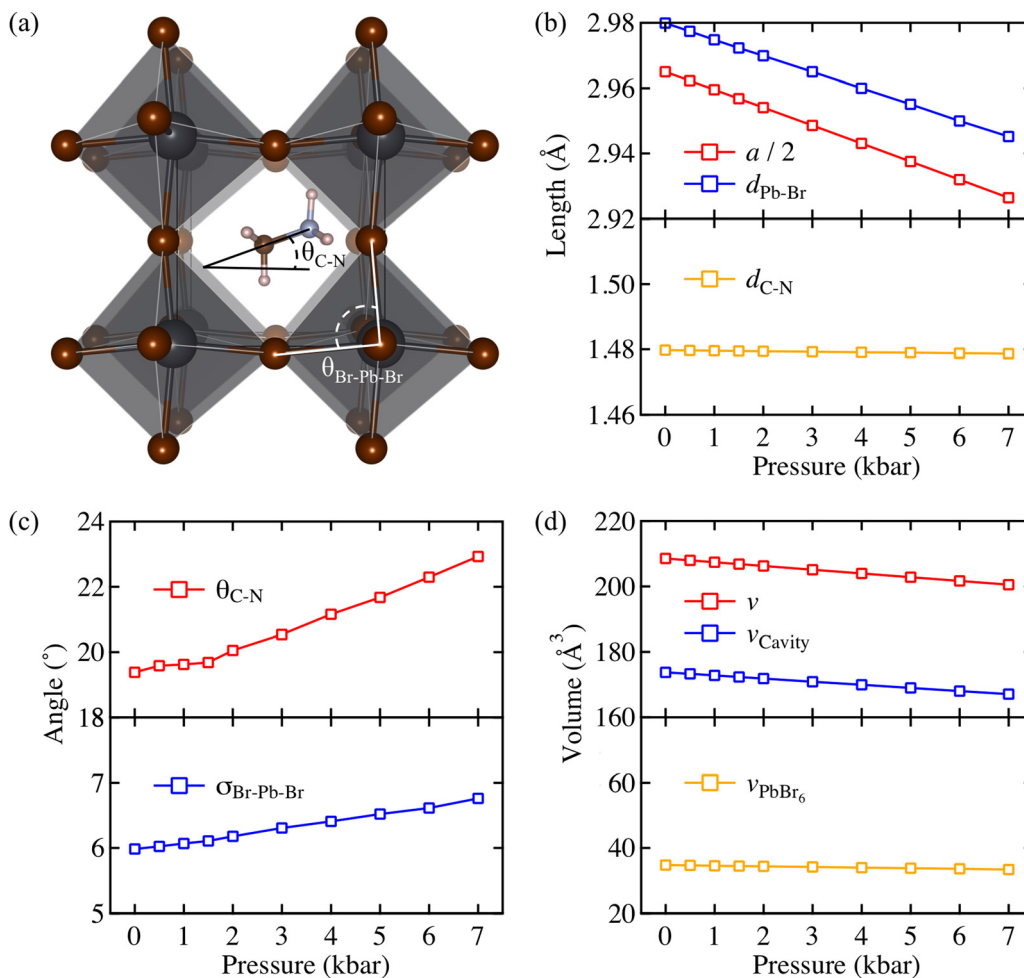
Fig. 2 (a) Atomic structure of MAPbBr$_3$, where the MA$^+$ molecule is oriented in the [110] direction on a (002) plane. θ_{C-N} is defined on ab-plane to describe the rotation of molecules within the cavity. Structural parameters in (b) length, (c) angle, and (d) volume dimension as a function of pressure. $a/2$, d_{Pb-Br}, and d_{C-N} stand for half of the lattice constant, averaged Pb–Br bond length, and C–N bond length in the unit cell, respectively. $\sigma_{Br-Pb-Br}$ denotes the standard deviation of the Br–Pb–Br bond angles deviated from the right angle (90°). ν and ν_{PbBr_6} are volume of the unit cell and PbBr$_6$ octahedron where $\nu_{Cavity} = \nu - \nu_{PbBr_6}$.

In our experimental settings, it is beyond our capabilities to obtain material specific properties such as change in crystal structure and defect concentration. Moreover, to attain insights into the causes of the observed quenching in EL intensity, it is necessary to decipher the origin of carrier recombination behavior at an atomic level; therefore, we performed first-principle DFT calculations. These are used to provide insights into the pressure-induced structural changes, as well as the impact of compression on defect formation to link with the macroscopic observation of EL quenching.

The optimised crystal structure of MAPbBr$_3$ is shown in Fig. 2a. The calculated lattice constant of $a_0 = 5.93$ Å coincides well with previously reported values of 5.91 Å (calculated)[22] and 5.94 Å (measured).[23] From fitting to the third-order Birch–Murnaghan equation-of-state,[24] a bulk modulus of $B_0 = 18.2$ GPa is obtained, which implies hybrid MAPbBr$_3$ is softer than inorganic CsPbBr$_3$ ($B_0 = 21.5$ GPa).[25] A report of $B_0 = 16.8$ GPa measured from Brillouin scattering is in good agreement.[26] Based on the calculated a_0 and B_0, the unit cell volume (ν) as a

function of pressure is obtained following

$$\nu = \nu_0 \left(1 - \frac{P}{B_0} \right) \qquad (1)$$

where ν_0 is the equilibrium volume of the unit cell at 0 pressure ($\nu_0 = (a_0)^3$) and P is applied pressure. According to Eqn 1 we compressed the volume of MAPbBr$_3$ unit cell isotropically (i.e. $a = \sqrt[3]{\nu}$) and fully relaxed the internal coordinates of all atoms. Changes of structural parameters as a function of pressure are plotted in Fig. 2b.

Unlike the ideal perovskite structure (e.g. cubic CsPbBr$_3$) where the Pb–Br bond length is half of its lattice constant, the averaged Pb–Br bond length of MAPbBr$_3$ (d_{Pb-Br}) in MAPbBr$_3$ is larger than $a/2$. This is because the MA$^+$ molecular cation allows internal distortion of PbBr$_6$ octahedron in MAPbBr$_3$. While d_{Pb-Br} shortens as more pressure is applied, the C–N bond length of MA$^+$ (d_{C-N}) remains constant, which means that the applied pressure mainly affects the 3-dimensional PbBr$_6$ octahedral networks and leaves the molecular cation unperturbed

due to its stiffer bond. As a result, internal distortion of the $PbBr_6$ octahedron becomes severe. A quantitative measure, the standard deviation of the octahedral angles ($\sigma_{Br-Pb-Br}$) defined by eqn (2),[27,28] is plotted as a function of pressure in Fig. 2c.

$$\sigma_{Br-Pb-Br} = \sqrt{\frac{\sum_{i=1}^{12} (\theta_{Br-Pb-Br,i} - 90°)^2}{11}} \qquad (2)$$

It confirms that pressure distorts the octahedra and consequently MA^+ rotates to fit in the cavity. It is notable that the volume of $PbBr_6$ is kept constant while the volume of the cavity shrinks under the pressure (see Fig. 2d). This could explain the microscopic origin of the organic cations locking under pressure that have been observed.[29]

Hybrid lead halide perovskites are known to exhibit Rashba splitting in their band dispersion due to a break of the centrosymmetry by the presence of the molecular cation.[30,31] To assess the impact of pressure on the electronic structure of $MAPbBr_3$ including its Rashba splitting, we sampled a dense 3D

k-point mesh near the R point in the momentum space. Fig. 3a depicts the band structure of $MAPbBr_3$ and physical quantities that can make quantitative analysis of Rashba splitting available. The evolution of actual band structures is plotted in Fig. S4 and S5 (ESI‡). Band gap values shown in Fig. 3b are underestimated with respect to our measurement due to the level of theory. The use of the generalised gradient approximation with relativistic corrections can capture correct trends in relative changes of atomic and electronic structures for halide perovskites.[28]

Both the indirect and direct band gap of $MAPbBr_3$ ($E_{g,indir}$) and ($E_{g,dir}$) decrease under applied pressure, Fig. 3b. This positive volume deformation potential (negative pressure coefficient) of the band gap arises through contributing the Pb 6s orbitals to the band structure.[32] The band gap shrinkage of $\sim$25 meV at 7 kbar from our calculation is in the same order as the EL peak shift of our device ($\sim$45 meV) at 7 kbar. When the band gap is simply measured right at the R point ($E_{g,R}$), it exhibits an opposite (increasing) trend as a function of the pressure, which means that sampling k-mesh properly near the
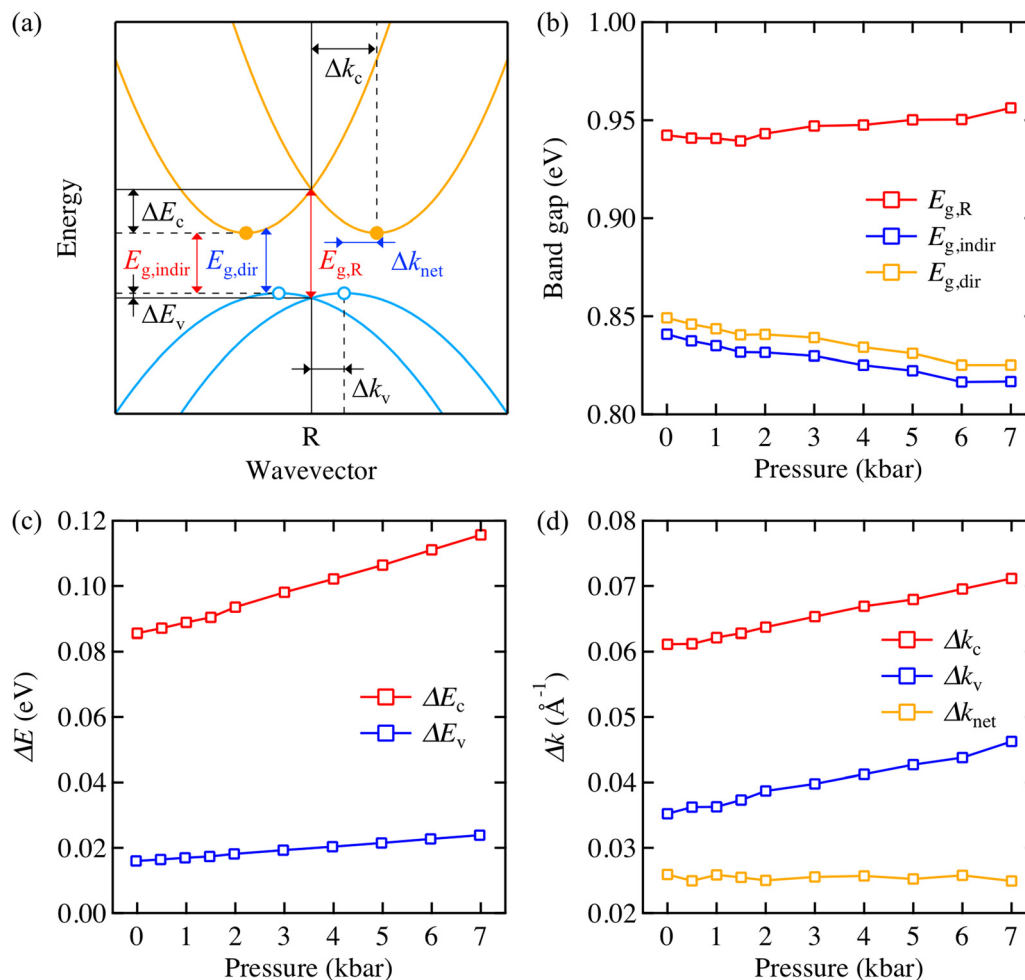
Fig. 3 (a) Schematic electronic band structure of $MAPbBr_3$ near the R point in energy-momentum space. Change of (b) DFT band gap, (c) eigenvalue, (d) momentum at band extrema as a function of pressure. $E_{g,R}$ stands for the band gap at R point, $E_{g,indir}$ and $E_{g,dir}$ are indirect and direct band gap. ΔE_c (ΔE_v) and Δk_c (Δk_v) denote eigenvalue and momentum difference between the R point and the conduction band minimum (valence band maximum), respectively. $\Delta k_{net} = \Delta k_c - \Delta k_v$.

This journal is © The Royal Society of Chemistry 2022

J. Mater. Chem. C, 2022, **10**, 12560–12568 | **12563**

high symmetry point is necessary to capture the Rashba splitting. We also note that the Rashba splitting mitigates band gap shrinkage (see Fig. S3, ESI‡).

We further analysed how the shape of the Rashba pockets evolves under pressure as the shape of band structure could impact charge carrier recombination dynamics.[21,33,34] Fig. 3c and d display that the actual band extrema drift apart from the R point both on the energy axis and momentum (wavevector) axis as pressure is applied, which indicates the Rashba pockets on the upper valence band and lower conduction band become deeper and wider under pressure. Exact band extrema positions in the reciprocal space and values used to plot Fig. 3c and d are tabulated in Table S1 (ESI‡). We attribute the shift of ΔE and Δk to the distortion of $PbBr_6$ octahdera under pressure, as the correlation between octahedral distortion and spin–orbit coupling has been previously reported in halide perovskite systems.[28,35,36] Nonetheless, it is important that the k-space separation between electrons and holes (represented by Δk_{net}) remains constant, since it implies a change in band structure does not result in the enhancement of phonon-assisted indirect

recombination that is a result of momentum mismatch. We conclude that the primary origin of the EL intensity decrease observed in our experiment is not related to the change of electronic structure. An interesting point is that no indirect to direct band gap transition occurs in $MAPbBr_3$ unlike previous reports from $MAPbI_3$.[21]

A correlation between strain and non-radiative recombination has been reported, where local defect density plays an important role.[14] To assess this effect, we sampled 6 charged vacancies and interstitials (i.e. $V_{MA}{}^-$, $V_{Pb}{}^{2-}$, $V_{Br}{}^+$, $MA_i{}^+$, $Pb_i{}^{2+}$, and $Br_i{}^-$) that can be found in $MAPbBr_3$. To quantify how applied pressure can affects defect population, we predicted a change in relative defect concentration of all vacancies and interstitials as a function of applied pressure following eqn (7). In Fig. 4a, concentration of Br anion vacancy is expected to increase ($\sim 10^7$ times at 7 kbar), while the concentration of MA and Pb cation vacancies is expected to decrease. In Fig. 4b, interstitial defects exhibit opposite tendencies, i.e. concentration of Br anion interstitial is predicted to decrease and concentration of the other cation interstitials are predicted to
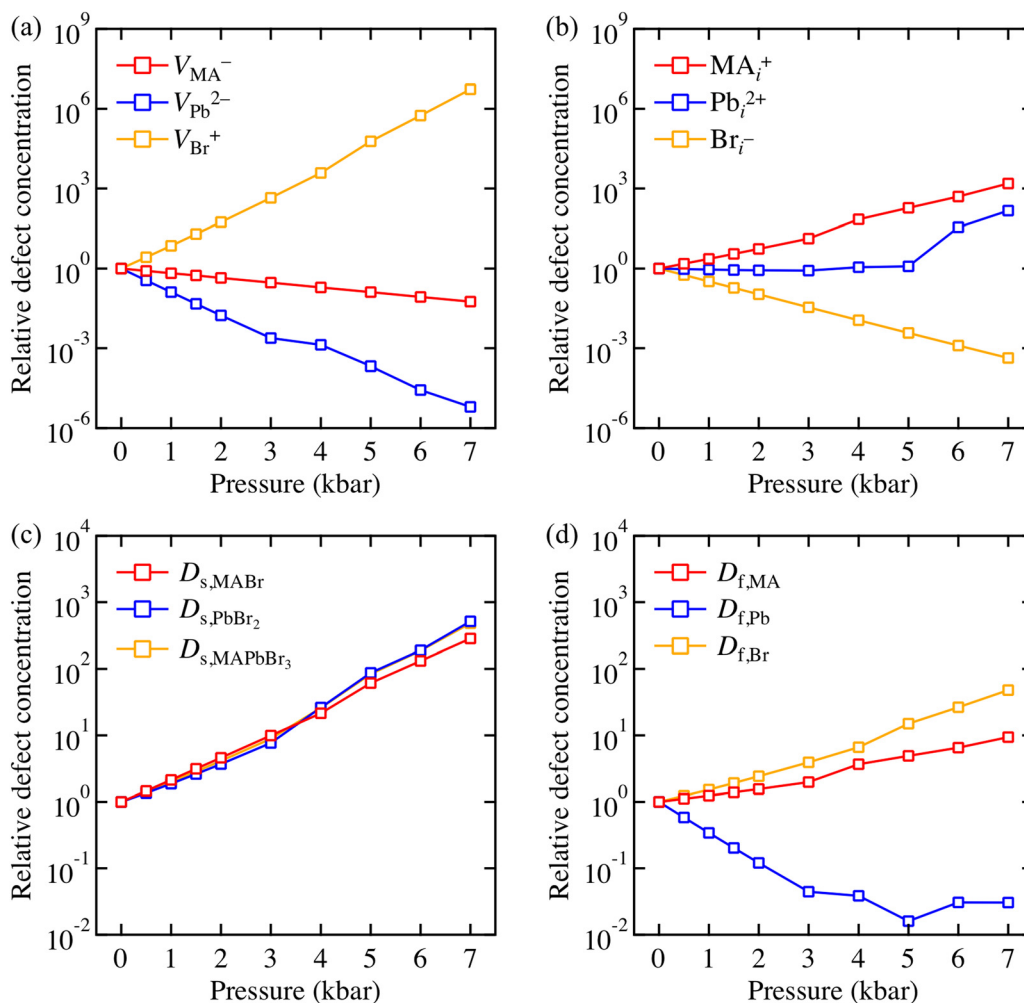

Fig. 4 Relative defect concentration of point defects in $MAPbBr_3$: (a) vacancies where $V_{MA}{}^-$, $V_{Pb}{}^{2-}$ and $V_{Br}{}^+$ stand for MA, Pb, and Br vacancy, (b) interstitials where $MA_i{}^+$, $Pb_i{}^{2+}$, and $Br_i{}^-$ stand for MA, Pb, and Br interstitial, (c) Schottky disorder where $D_{s,MABr}$, $D_{s,PbBr_2}$, and $D_{s,MAPbBr_3}$ denote MABr, PbBr2, and, MAPbBr3 Schottky pair, and (d) frenkel disorder where $D_{f,MA}$, $D_{f,Pb}$, and $D_{f,Br}$ denote Frenkel pair.

12564 | *J. Mater. Chem. C*, 2022, **10**, 12560–12568

This journal is © The Royal Society of Chemistry 2022

Table 1 Calculated formation energy of Schottky and Frenkel defects in MAPbBr$_3$ (ΔH_d) from DFT for a $2 \times 2 \times 2$ pseudo-cubic supercell

	Reaction	ΔH_d (eV defect^{-1})
Schottky	Nil $\rightarrow V_{MA}{}^{-} + V_{Br}{}^{+} + MABr$	0.14
Disorder	Nil $\rightarrow V_{Pb}{}^{2-} + 2\,V_{Br}{}^{+} + PbBr_2$	0.24
	Nil $\rightarrow V_{MA}{}^{-} + V_{Pb}{}^{2-} + 3V_{Br}{}^{+} + MAPbBr_3$	0.20
Frenkel	Nil $\rightarrow V_{MA}{}^{-} + MA_i{}^{+}$	0.07
Disorder	Nil $\rightarrow V_{Pb}{}^{2-} + Pb_i{}^{2+}$	2.15
	Nil $\rightarrow V_{Br}{}^{+} + Br_i{}^{-}$	0.24

increase. Here, it is found that $V_{Br}{}^{+}$ is the most pressure-sensitive defect species.

The predictions shown in Fig. 4a and b assume local equilibrium at each pressure point, which is reasonable considering the relatively high ion mobility at in these materials at room temperature. Once an ion escapes from its lattice site and forms a vacancy, this ion can induce another vacancy to compensate the charge (Schottky disorder) or form an interstitial (Frenkel disorder).[37] Possible balanced defect reactions are summarised in Table 1. The partial and full Schottky defect formation energies of MAPbBr$_3$ are similar to previously reported values of MAPbI$_3$,[38] which implies that Schottky disorder is common in bromide perovskites, as well as iodide perovskites. Interestingly, MA and Br Frenkel disorder is found to be as accessible as Schottky disorder, whilst Pb Frenkel disorder is energetically unfavourable.

The variation of defect concentrations under pressure is shown in Fig. 4c and d, respectively. Schottky disorder is expected to increase up to 1000 times at 7 kbar. MA and Br Frenkel disorder is also predicted to increase, whereas Pb Frenkel disorder is predicted to decrease. The driving force behind the enhancement of Schottky and Br Frenkel disorders is stabilisation of Br anion vacancy under compression – in other words, reduction of $V_{Br}{}^{+}$ formation energy overcomes the rise of $V_{MA}{}^{-}$, $V_{Pb}{}^{2-}$, and Br$_i{}^{-}$ formation energies. On the other hand, the driving force behind the enhancement of MA Frenkel disorder is stabilisation of the MA interstitial.

An increase in crystal disorder, with a distribution of charged defect centres, will enhance carrier trapping due to band edge fluctuations in the semiconducting crystal. Furthermore, both the Br vacancy and interstitial introduce trap states within the band gap.[39,40] These effects, which arise from enhanced Schottky disorder and Br Frenkel disorder under pressure, will lead to non-radiative pathways that lower the LED efficiency. In addition to bulk processes, pressure-induced changes at surfaces,[41] interfaces,[42,43] and grain boundaries can may also play a role, but are beyond the scope of this investigation.

Conclusions

The change in optoelectronic and material properties of MAPbBr$_3$, probed using a combination of simulation techniques and experimental measurements, highlights that: (i) pressure distorts PbBr$_6$ octahedra in the MAPbBr$_3$ crystal, which results in larger relativistic Rashba splitting with electron and

hole pockets near the R point that are deeper and wider; (ii) the band gap is reduced under hydrostatic pressure with indirectness of the band gap unchanged, which explains the red-shifted EL observed in MAPbBr$_3$ LEDs; (iii) both Schottky and Frenkel disorder is enhanced under hydrostatic pressure, which leads to an increase in charged defect populations and a decrease in EL intensity. The same processes that we observe for pressure-induced behaviour are expected to be relevant for strain effects in general where the local structure is expanded or compressed, including carrier recombination phenomena related to photostriction,[44,45] phase transitions,[14,46] and compositional gradients.[47,48]

Experimental methods

Sample preparation

The following chemicals were supplied from MABr and PbBr$_2$ (>99%, Sigma-Aldrich), and F8 was provided by Cambridge Display Technology (CDT) Ltd. All materials were used as received from their sources without further purification. For the methylammonium lead tribromide (CH$_3$NH$_3$PbBr$_3$, MAPbBr$_3$) perovskite precursor solution (37.8 wt%), MABr and PbBr$_2$ with a molar ratio of 1:1 were dissolved in a cosolvent of N,N-dimethylformamide (DMF) with 6 vol% of an aqueous hydrobromic acid (HBr) (48 wt%). The LED device was fabricated according to the recipe given in ref. 17. The LED was fabricated on a pre-patterned indium tin oxide (ITO) substrate that was cleaned in an ultrasonic bath with acetone, 2-propanol and followed by treatment in an oxygen-plasma etcher for 10 min, sequentially. A thin layer of poly(3,4-ethylenedioxythiophene) polystyrene sulfonic acid (PEDOT:PSS) was used as the hole transport layer (HTL) which was spun coated at 5000 rpm for 45 s on the substrate and then baked at 140 °C for 10 min under nitrogen atmosphere. Subsequently, the MAPbBr$_3$ precursor solution was spun coated onto the PEDOT:PSS layer at 3000 rpm for 60 s and followed by annealing at 100 °C for 2 h. The Poly(9,9-di-n-octylfluorenyl-2,7-diyl) (F8) polymer solution with a concentration of (0.8 mg ml^{-1} in
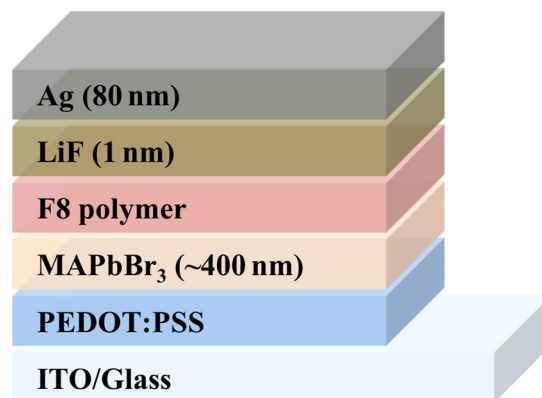
Fig. 5 Schematic device structure of MAPbBr$_3$ based LED, with (ITO/PEDOT:PSS/MAPbBr$_3$/LiF/Ag) architecture. The active area of the device was 1 mm^2.

chlorobenzene) was spun coated onto the perovskite layer at 3000 rpm for 60 s. The device fabrication is concluded by thermally evaporating approximately 1 nm of LiF, followed by 80 nm of Ag. The device was fabricated, had wires attached to it, was encapsulated inside a N2-filled glove-box, and had an active area of 1 mm^2 which was defined using a mask. Schematic of the device is shown in Fig. 5.

EL Measurement under hydrostatic pressure

The measurements of EL spectra as a function of pressure dependence were carried out at room temperature using the capillary-fed piston-cylinder cell pressure system with a manganin coil acting as a pressure gauge.[49] The LED was immersed within the cell in 3MTM FluorinertTM (FC-77) liquid, which is characterised by being very inert with high electrical resistivity (1.9×10^{15} Ω cm) and is employed as a hydrostatic pressure transferring medium.[50] The electroluminescence (EL) spectra emitted from the LED were recorded using a spectrometer positioned outside the pressure cell. During the measurements, the device was operated at a constant current while the light emitted was simultaneously collected and transmitted through an optical fiber from the device within the cell to the spectrometer. The collection of light emitted vertically to the substrate was achieved through having one port of thefibre located close to the sample. The pressure was increased gradually from ambient to 8 kbar in steps of 0.5 kbar. The EL was recorded using a fiber-coupled USB2000 Spectrometer with SpectraSuite software from Ocean Optics, while driving the LED at a constant current using a Keithley 2400 source measurement unit.

Bulk structure calculations

Calculations were performed based on Kohn–Sham density-functional theory[51] for a series of 10 pressures. The Vienna Ab Initio Simulation Package (VASP)[52,53] was used with projector augmented-wave (PAW)[54,55] scalar-relativistic potentials. The valence states of H, C, N, Br, and Pb are treated explicitly by $1(1s^1)$, $4 (2s^2 2p^2)$, $5(2s^2 2p^3)$, $7(4s^2 4p^5)$, and $14(5d^{10} 6s^2 6p^2)$ electrons, respectively. For structure optimization, the Perdew–Burke–Ernzerhof exchange-correlation functional revised for solids (PBEsol)[56] was employed with the plane-wave kinetic cutoff energy of 700 eV. High convergence criteria of 10^{-6} eV for total energy in the unit cell and 10^{-3} eV Å^{-1} for forces on each atom were set to properly describe the change in atomic structures under small volume changes.

For the primitive unit cell, a Γ-centred k-point grid of $8 \times 8 \times 8$ was used. To obtain accurate values of valence band maximum (VBM) and conduction band minimum (CBM) in energy-momentum space, a fine k-point mesh near the R point $(0.5, 0.5, 0.5)$ was sampled in two steps: (i) $13 \times 13 \times 13$ mesh within $|k_i - R| \leq 0.06[2\pi/a_0]$, where $i = x$, y, and z; (ii) $13 \times 13 \times 13$ mesh within $|k_i - R'| \leq 0.006[2\pi/a_0]$, where R' is the point that has minimum (maximum) eigenvalue from the first step. The rest of the Brillouin zone was sampled on $8 \times 8 \times 8$ mesh. Spin–orbit coupling (SOC) was included to describe the splitting of band edges.

Defect thermodynamics

Within the modern theory of point defects in crystals, the enthalpy of defect formation ($\Delta H_{\alpha,q}^{\text{defect}} (\mu_i, E_{\text{F}})$) be calculated as a function of chemical potential (μ_i) and Fermi level (E_{F}) following

$$\Delta H_{\alpha,q}^{\text{defect}}(\mu_i, E_{\text{F}}) = E_{\alpha,q}^{\text{defect}} - E^{\text{host}} + \sum_i \mu_i + q E_{\text{F}} \quad (3)$$

where $E_{\alpha,q}^{\text{defect}}$ and E^{host} are the total energy of a $2 \times 2 \times 2$ supercell with point defect α in charge state q and a perfect supercell, respectively.[57,58] To consider the effect of strain (ε) on defect formation, we assumed that strain only affects the total energy and re-formulated eqn (3) to

$$\Delta H_{\alpha,q}^{\text{defect}}(\mu_i, E_{\text{F}}, \epsilon) = E_{\alpha,q}^{\text{defect}}(\epsilon) - E^{\text{host}}(\epsilon) + \sum_i \mu_i + q E_{\text{F}} \quad (4)$$

where $E_{\alpha,q}^{\text{defect}}(\varepsilon)$ and $E^{\text{host}}(\varepsilon)$ are the total energy of a strained supercell with point defect α in charge state q and a perfect strained supercell. From Eqn 4, the relative defect concentration of strained crystal to unstrained crystal ($n_{\alpha,q}^{\text{defect}} (\varepsilon) / n_{\alpha,q}^{\text{defect}} (0)$) can be defined following

$$\frac{n_{\alpha,q}^{\text{defect}}(\epsilon)}{n_{\alpha,q}^{\text{defect}}(0)} = \frac{\exp\left[-\dfrac{\Delta H_{\alpha,q}^{\text{defect}}(\mu_i, E_F, \epsilon)}{k_{\text{B}} T}\right]}{\exp\left[-\dfrac{\Delta H_{\alpha,q}^{\text{defect}}(\mu_i, E_F, 0)}{k_{\text{B}} T}\right]} \quad (5)$$

$$= \exp\left[-\frac{\Delta H_{\alpha,q}^{\text{defect}}(\mu_i, E_F, \epsilon) - \Delta H_{\alpha,q}^{\text{defect}}(\mu_i, E_F, 0)}{k_{\text{B}} T}\right] \quad (6)$$

$$= \exp\left[-\frac{\left(E_{\alpha,q}^{\text{defect}}(\epsilon) - E^{\text{host}}(\epsilon)\right) - \left(E_{\alpha,q}^{\text{defect}}(0) - E^{\text{host}}(0)\right)}{k_{\text{B}} T}\right] \quad (7)$$

where k_{B} and T are Boltzmann constant and temperature, respectively. This means that the change in the relative defect concentration can be calculated from the total energy differences as the chemical potentials cancel. We note that change in charged defect correction term is found to be negligible at the given pressure range (see Fig. S6, ESI‡).

Author contributions

Y.-K. J. and A. M. equally contributed to this work and performed the primary modelling and measurements, respectively. All authors contributed to discussing the results and writing the manuscript.

Conflicts of interest

The authors declare no competing financial interests.

Acknowledgements

12566 | *J. Mater. Chem. C*, 2022, **10**, 12560–12568

This journal is © The Royal Society of Chemistry 2022

References

1 A. Kojima, K. Teshima, Y. Shirai and T. Miyasaka, Organo-metal Halide Perovskites as Visible-Light Sensitizers for Photovoltaic Cells, *J. Am. Chem. Soc.*, 2009, **131**, 6050–6051.

2 H.-S. Kim, C.-R. Lee, J.-H. Im, K.-B. Lee, T. Moehl, A. Marchioro, S.-J. Moon, R. Humphry-Baker, J.-H. Yum and J. E. Moser, *et al.*, Lead iodide perovskite sensitized all-solid-state submicron thin film mesoscopic solar cell with efficiency exceeding 9%, *Sci. Rep.*, 2012, **2**, 1–7.

3 Z.-K. Tan, R. S. Moghaddam, M. L. Lai, P. Docampo, R. Higler, F. Deschler, M. Price, A. Sadhanala, L. M. Pazos and D. Credgington, *et al.*, Bright light-emitting diodes based on organometal halide perovskite, *Nat. Nanotechnol.*, 2014, **9**, 687–692.

4 L. N. Quan, B. P. Rand, R. H. Friend, S. G. Mhaisalkar, T.-W. Lee and E. H. Sargent, Perovskites for Next-Generation Optical Sources, *Chem. Rev.*, 2019, **119**, 7444–7477.

5 NREL, Best Research-Cell Efficiencies. https://www.nrel.gov/pv/cell-efficiency.html, (accessed March 16, 2022).

6 M. Jeong, I. W. Choi, E. M. Go, Y. Cho, M. Kim, B. Lee, S. Jeong, Y. Jo, H. W. Choi and J. Lee, *et al.*, Stable perovskite solar cells with efficiency exceeding 24.8% and 0.3-V voltage loss, *Science*, 2020, **369**, 1615–1620.

7 K. Lin, J. Xing, L. N. Quan, F. P. G. de Arquer, X. Gong, J. Lu, L. Xie, W. Zhao, D. Zhang and C. Yan, *et al.*, Perovskite light-emitting diodes with external quantum efficiency exceeding 20 per cent, *Nature*, 2018, **562**, 245–248.

8 B. Zhao, S. Bai, V. Kim, R. Lamboll, R. Shivanna, F. Auras, J. M. Richter, L. Yang, L. Dai and M. Alsari, *et al.*, High-efficiency perovskite–polymer bulk heterostructure light-emitting diodes, *Nat. Photonics*, 2018, **12**, 783–789.

9 S. D. Stranks, Nonradiative Losses in Metal Halide Perovskites, *ACS Energy Lett.*, 2017, **2**, 1515–1525.

10 J.-S. Park, S. Kim, Z. Xie and A. Walsh, Point defect engineering in thin-film solar cells, *Nat. Rev. Mater.*, 2018, **3**, 194–210.

11 J. N. Wilson, J. M. Frost, S. K. Wallace and A. Walsh, Dielectric and ferroic properties of metal halide perovskites, *APL Mater.*, 2019, **7**, 010901.

12 D. Liu, D. Luo, A. N. Iqbal, K. W. Orr, T. A. Doherty, Z.-H. Lu, S. D. Stranks and W. Zhang, Strain analysis and engineering in halide perovskite photovoltaics, *Nat. Mater.*, 2021, **20**, 1337–1346.

13 D. W. de Quilettes, S. M. Vorpahl, S. D. Stranks, H. Nagaoka, G. E. Eperon, M. E. Ziffer, H. J. Snaith and D. S. Ginger, Impact of microstructure on local carrier lifetime in perovskite solar cells, *Science*, 2015, **348**, 683–686.

14 T. W. Jones, A. Osherov, M. Alsari, M. Sponseller, B. C. Duck, Y.-K. Jung, C. Settens, F. Niroui, R. Brenes and C. V. Stan, *et al.*, Lattice strain causes non-radiative losses in halide perovskites, *Energy Environ. Sci.*, 2019, **12**, 596–606.

15 G. Kim, H. Min, K. S. Lee, S. M. Yoon and S. I. Seok, Impact of strain relaxation on performance of α-formamidinium lead iodide perovskite solar cells, *Science*, 2020, **370**, 108–112.

16 T. Ye, K. Wang, S. Ma, C. Wu, Y. Hou, D. Yang, K. Wang and S. Priya, Strain-relaxed tetragonal MAPbI$_3$ results in efficient mesoporous solar cells, *Nano Energy*, 2021, **83**, 105788.

17 J. C. Yu, D. B. Kim, E. D. Jung, B. R. Lee and M. H. Song, High-performance perovskite light-emitting diodes via morphological control of perovskite films, *Nanoscale*, 2016, **8**, 7036–7042.

18 K. Matsuishi, T. Ishihara, S. Onari, Y. Chang and C. Park, Optical properties and structural phase transitions of lead-halide based inorganic-organic 3D and 2D perovskite semi-conductors under high pressure, *Phys. Status Solidi B*, 2004, **241**, 3328–3333.

19 A. Jaffe, Y. Lin, C. M. Beavers, J. Voss, W. L. Mao and H. I. Karunadasa, High-pressure single-crystal structures of 3D lead-halide hybrid perovskites and pressure effects on their electronic and optical properties, *ACS Cent. Sci.*, 2016, **2**, 201–209.

20 X. Lü, W. Yang, Q. Jia and H. Xu, Pressure-induced dramatic changes in organic-inorganic halide perovskites, *Chem. Sci.*, 2017, **8**, 6764–6776.

21 T. Wang, B. Daiber, J. M. Frost, S. A. Mann, E. C. Garnett, A. Walsh and B. Ehrler, Indirect to direct bandgap transition in methylammonium lead halide perovskite, *Energy Environ. Sci.*, 2017, **10**, 509–515.

22 F. Brivio, C. Caetano and A. Walsh, Thermodynamic Origin of Photoinstability in the $CH_3NH_3Pb(I_{1-x}Br_x)_3$ Hybrid Halide Perovskite Alloy, *J. Phys. Chem. Lett.*, 2016, **7**, 1083–1087.

23 G. Kieslich, J. M. Skelton, J. Armstrong, Y. Wu, F. Wei, K. L. Svane, A. Walsh and K. T. Butler, Hydrogen Bonding versus Entropy: Revealing the Underlying Thermodynamics of the Hybrid Organic–Inorganic Perovskite $[CH_3NH_3]PbBr_3$, *Chem. Mater.*, 2018, **30**, 8782–8788.

24 F. Birch, Finite Elastic Strain of Cubic Crystals, *Phys. Rev.*, 1947, **71**, 809–824.

25 Y.-K. Jung, K. T. Butler and A. Walsh, Halide Perovskite Heteroepitaxy: Bond Formation and Carrier Confinement at the PbS–CsPbBr$_3$ Interface, *J. Phys. Chem. C*, 2017, **121**, 27351–27356.

26 A. C. Ferreira, A. Létoublon, S. Paofai, S. Raymond, C. Ecolivet, B. Rufflé, S. Cordier, C. Katan, M. I. Saidaminov and A. A. Zhumekenov, *et al.*, Elastic Softness of Hybrid Lead Halide Perovskites, *Phys. Rev. Lett.*, 2019, **121**, 085502.

27 K. Robinson, G. V. Gibbs and P. H. Ribbe, Quadratic Elongation: A Quantitative Measure of Distortion in Coordination Polyhedra, *Science*, 1971, **172**, 567–570.

28 X. Zhang, J.-X. Shen, W. Wang and C. G. Van de Walle, First-Principles Analysis of Radiative Recombination in Lead-Halide Perovskites, *ACS Energy Lett.*, 2018, **3**, 2329–2334.

This journal is © The Royal Society of Chemistry 2022

J. Mater. Chem. C, 2022, **10**, 12560–12568 | **12567**

29 A. Francisco-López, B. Charles, O. J. Weber, M. I. Alonso, M. Garriga, M. Campoy-Quiles, M. T. Weller and A. R. Goñi, Pressure-Induced Locking of Methylammonium Cations versus Amorphization in Hybrid Lead Iodide Perovskites, *J. Phys. Chem. C*, 2018, **122**, 22073–22082.

30 D. Niesner, M. Wilhelm, I. Levchuk, A. Osvet, S. Shrestha, M. Batentschuk, C. Brabec and T. Fauster, Giant Rashba Splitting in $CH_3NH_3PbBr_3$ Organic-Inorganic Perovskite, *Phys. Rev. Lett.*, 2016, **117**, S156.

31 L. D. Whalley, J. M. Frost, Y.-K. Jung and A. Walsh, Perspective: Theory and simulation of hybrid halide perovskites, *J. Chem. Phys.*, 2017, **146**, 220901–220912.

32 J. M. Frost, K. T. Butler, F. Brivio, C. H. Hendon, M. van Schilfgaarde and A. Walsh, Atomistic Origins of High-Performance in Hybrid Halide Perovskite Solar Cells, *Nano Lett.*, 2014, **14**, 2584–2590.

33 S. D. Stranks and P. Plochocka, The influence of the Rashba effect, *Nat. Mater.*, 2018, **17**, 381–382.

34 X. Zhang, J.-X. Shen and C. G. Van de Walle, First-Principles Simulation of Carrier Recombination Mechanisms in Halide Perovskites, *Adv. Energy Mater.*, 2019, **10**, 1902830.

35 A. Amat, E. Mosconi, E. Ronca, C. Quarti, P. Umari, M. K. Nazeeruddin, M. Grätzel and F. De Angelis, Cation-Induced Band-Gap Tuning in Organohalide Perovskites: Interplay of Spin–Orbit Coupling and Octahedra Tilting, *Nano Lett.*, 2014, **14**, 3608–3616.

36 Y.-K. Jung, J.-H. Lee, A. Walsh and A. Soon, Influence of Rb/Cs Cation-Exchange on Inorganic Sn Halide Perovskites: From Chemical Structure to Physical Properties, *Chem. Mater.*, 2017, **29**, 3181–3188.

37 E. Mosconi, D. Meggiolaro, H. J. Snaith, S. D. Stranks and F. De Angelis, Light-induced annihilation of Frenkel defects in organo-lead halide perovskites, *Energy Environ. Sci.*, 2016, **9**, 3180–3187.

38 A. Walsh, D. O. Scanlon, S. Chen, X.-G. Gong and S.-H. Wei, Self-regulation mechanism for charged point defects in hybrid halide perovskites, *Angew. Chem., Int. Ed.*, 2015, **54**, 1791–1794.

39 A. Mannodi-Kanakkithodi, J.-S. Park, A. B. Martinson and M. K. Chan, Defect Energetics in Pseudo-Cubic Mixed Halide Lead Perovskites from First-Principles, *J. Phys. Chem. C*, 2020, **124**, 16729–16738.

40 X. Zhang, M. E. Turiansky, J.-X. Shen and C. G. Van de Walle, Iodine interstitials as a cause of nonradiative recombination in hybrid perovskites, *Phys. Rev. B: Condens. Matter Mater. Phys.*, 2020, **101**, 140101.

41 Y. Fang, Q. Dong, Y. Shao, Y. Yuan and J. Huang, Highly narrowband perovskite single-crystal photodetectors enabled by surface-charge recombination, *Nat. Photonics*, 2015, **9**, 679–686.

42 K. K. Wong, A. Fakharuddin, P. Ehrenreich, T. Deckert, M. Abdi-Jalebi, R. H. Friend and L. Schmidt-Mende, Interface-Dependent Radiative and Nonradiative Recombination in Perovskite Solar Cells, *J. Phys. Chem. C*, 2018, **122**, 10691–10698.

43 C. M. Wolff, P. Caprioglio, M. Stolterfoht and D. Neher, Nonradiative Recombination in Perovskite Solar Cells: The Role of Interfaces, *Adv. Mater.*, 2019, **31**, 1902762.

44 Y. Zhou, S. Wang, Z. Ku, H. Fan, D. Schmidt, A. Rusydi, L. Chang, L. Wang, P. Ren and L. Chen, *et al.*, Giant photostriction in organic–inorganic lead halide perovskites, *Nat. Commun.*, 2016, **7**, 1–8.

45 H. Tsai, R. Asadpour, J. C. Blancon, C. C. Stoumpos, O. Durand, J. W. Strzalka, B. Chen, R. Verduzco, P. M. Ajayan and S. Tretiak, *et al.*, Light-induced lattice expansion leads to high-efficiency perovskite solar cells, *Science*, 2018, **360**, 67–70.

46 I. M. Hermes, S. A. Bretschneider, V. W. Bergmann, D. Li, A. Klasen, J. Mars, W. Tremel, F. Laquai, H. J. Butt and M. Mezger, *et al.*, Ferroelastic Fingerprints in Methylammonium Lead Iodide Perovskite, *J. Phys. Chem. C*, 2016, **120**, 5724–5731.

47 D. P. McMeekin, Z. Wang, W. Rehman, F. Pulvirenti, J. B. Patel, N. K. Noel, M. B. Johnston, S. R. Marder, L. M. Herz and H. J. Snaith, Crystallization Kinetics and Morphology Control of Formamidinium-Cesium Mixed-Cation Lead Mixed-Halide Perovskite via Tunability of the Colloidal Precursor Solution, *Adv. Mater.*, 2017, **29**, 1607039.

48 C. Zhu, X. Niu, Y. Fu, N. Li, C. Hu, Y. Chen, X. He, G. Na, P. Liu and H. Zai, *et al.*, Strain engineering in perovskite solar cells and its impacts on carrier dynamics, *Nat. Commun.*, 2019, **10**, 1–11.

49 D. Guy and R. Friend, Temperature measurement in high pressure cells using a rhodium +0.5% iron-chromel thermo-couple pair, *J. Phys. E: Sci. Instrum.*, 1986, **19**, 430.

50 T. Varga, A. P. Wilkinson and R. J. Angel, Fluorinert as a pressure-transmitting medium for high-pressure diffraction studies, *Rev. Sci. Instrum.*, 2003, **74**, 4564–4566.

51 W. Kohn and L. J. Sham, Self-Consistent Equations Including Exchange and Correlation Effects, *Phys. Rev.*, 1965, **140**, A1133–A1138.

52 G. Kresse and J. Furthmüller, Efficient Iterative Schemes for *Ab Initio* Total-Energy Calculations Using a Plane-Wave Basis Set, *Phys. Rev. B: Condens. Matter Mater. Phys.*, 1996, **54**, 11169–11186.

53 G. Kresse and J. Furthmüller, Efficiency of *Ab-Initio* Total Energy Calculations for Metals and Semiconductors Using a Plane-Wave Basis Set, *Comput. Mater. Sci.*, 1996, **6**, 15–50.

54 G. Kresse and D. Joubert, From Ultrasoft Pseudopotentials to the Projector Augmented-Wave Method, *Phys. Rev. B: Condens. Matter Mater. Phys.*, 1999, **59**, 1758–1775.

55 P. E. Blöchl, Projector Augmented-Wave Method, *Phys. Rev. B: Condens. Matter Mater. Phys.*, 1994, **50**, 17953–17979.

56 J. P. Perdew, A. Ruzsinszky, G. I. Csonka, O. A. Vydrov, G. E. Scuseria, L. A. Constantin, X. Zhou and K. Burke, Restoring the density-gradient expansion for exchange in solids and surfaces, *Phys. Rev. Lett.*, 2008, **100**, 136406.

57 C. Freysoldt, B. Grabowski, T. Hickel, J. Neugebauer, G. Kresse, A. Janotti and C. G. Van de Walle, First-principles calculations for point defects in solids, *Rev. Mod. Phys.*, 2014, **86**, 253–305.

58 A. Walsh and A. Zunger, Instilling defect tolerance in new compounds, *Nat. Mater.*, 2017, **16**, 964–967.

12568 | *J. Mater. Chem. C*, 2022, **10**, 12560–12568

This journal is © The Royal Society of Chemistry 2022